

## Excitation of longitudinal and transverse coherent acoustic phonons in nanometer free-standing films of (001) Si

Maher Harb,<sup>1</sup> Weina Peng,<sup>2</sup> Germán Sciaini,<sup>1</sup> Christoph T. Hebeisen,<sup>1</sup> Ralph Ernstorfer,<sup>1,\*</sup> Mark A. Eriksson,<sup>2</sup> Max G. Lagally,<sup>2</sup> Sergei G. Kruglik,<sup>1</sup> and R. J. Dwayne Miller<sup>1,†</sup>

<sup>1</sup>*Departments of Chemistry and Physics, and Institute for Optical Sciences, University of Toronto, 80 St. George Street, Toronto, Ontario, Canada M5S 3H6*

<sup>2</sup>*University of Wisconsin-Madison, Madison, Wisconsin 53706, USA*

(Received 18 September 2008; revised manuscript received 12 January 2009; published 9 March 2009)

Transmission electron diffraction is naturally sensitive to the detection of shear-type deformations in single-crystalline structures due to the effective tilting of the lattice planes characteristic of shear, but in general is insensitive to longitudinal phonon propagation. Here, we report on the generation and detection of both transverse and longitudinal coherent acoustic phonons in 33 nm free-standing (001)-oriented single crystalline Si films using femtosecond electron diffraction (FED) to monitor these laser-induced atomic displacements. The mechanism for excitation of the shear mode that leads to coupling to the longitudinal phonon is attributed to the inhomogeneous lateral profile of the optical-pump pulse and the periodic boundary condition imposed by the supporting grid structure. In this application, the constructive interference in the diffraction process makes FED particularly sensitive to the detection of coherent phonon modes and offers an atomic perspective of the dynamics involving collective motions.

DOI: [10.1103/PhysRevB.79.094301](https://doi.org/10.1103/PhysRevB.79.094301)

PACS number(s): 63.22.Dc, 61.05.J-, 43.35.+d

### I. INTRODUCTION

By studying the propagation of acoustic waves in nanostructures, one can reveal a wealth of information on the elastic properties of these structures. Given the typical speed of sound in solids of  $\sim 5$  km/s and the involvement of nanometer length scales, the expected period of oscillation of such coherent vibrations is in the picosecond range. The initiation of such oscillations and subsequent detection in the time domain are possible using a variety of methods that utilize ultrafast optical pulses. Among these, a simple and extensively employed technique is based on photoinducing thermoelastic stress in the structure.<sup>1-3</sup> Consider a thin film, impulsively excited by an ultrashort laser pulse. As the optical pulse duration is relatively short with respect to the time scale of thermal expansion, the film surface becomes stressed. Stress is relieved by launching acoustic strain waves, which propagate back and forth along the surface normal, partially reflecting off the film boundaries due to the mismatch in acoustic impedance. Propagating strain waves correspond to coherent atomic vibrations that modulate the optical properties of the film (e.g., the reflectivity), and could therefore be probed by a second optical pulse in the usual pump-probe arrangement. Ideally, one would like to be able to characterize both transverse and longitudinal-acoustic phonon modes in order to gain access to different components of the elastic-stiffness tensor of the material. However, such experiments are generally limited to the generation of longitudinal polarizations of acoustic waves. This limitation is mainly due to the homogeneous excitation lateral to the plane, as the dimensions of the pump pulse are usually orders of magnitude larger than its penetration depth. In particular, the homogeneous illumination of an isotropic crystal generates spherical acoustic point sources at the surface for each position corresponding to an absorbed photon, which together form a longitudinal wave front (see Ref. 4 for an

illustration of this effect). Recently, however, a few studies reported the successful generation and detection of transverse-acoustic waves. Matsuda *et al.*<sup>5</sup> excited shear waves in Zn and GaAs by using crystal surfaces asymmetrically cut at  $>20^\circ$ . The role of crystal orientation on the initiation of the shear mode was examined by Pezeril *et al.*<sup>4,6</sup> through both experiment and numerical solution of the acoustic wave equations. Rossignol *et al.*,<sup>7</sup> on the other hand, excited shear waves in Al by tightly focusing the pump beam down to  $1-2 \mu\text{m}$ , thereby reducing the directivity of the optoacoustic source. It must be noted that there exist other mechanisms by which it is possible to excite acoustic shear waves (for example, stimulated Brillouin scattering<sup>8</sup>). However, for the most part, these mechanisms involve multiple pump beams and require specific excitation geometries.

Alternatively, coherent vibrations can be detected with direct probes of structure such as electrons and x rays. In this scheme, the optical probe pulse is replaced by an electron (or an x ray) pulse, which probes displacements in the periodic structure at the atomic level by diffracting off the sample. In this context, several time resolved electron<sup>9</sup> and x-ray<sup>10-16</sup> experiments demonstrated the excitation and detection of longitudinal coherent acoustic phonons in thin films and superlattice structures. However, to date, it has not been possible to resolve the transverse-acoustic components primarily due to signal-to-noise limitations. In this study, we use femtosecond electron diffraction (FED) to detect both longitudinal and shear acoustic waves in (001)-oriented single-crystalline Si. The technique marks a departure from the existing methods, which tackle the difficulty of exciting shear phonons by enhancing the initiation mechanism. Instead, we exploit the great sensitivity of electron diffraction to detect coherent transverse motions in single crystals, as demonstrated here for (001)-oriented Si with less than  $0.2^\circ$  of surface miscut. The use of single crystals rather than polycrystalline samples greatly enhances the signal-to-noise ratio

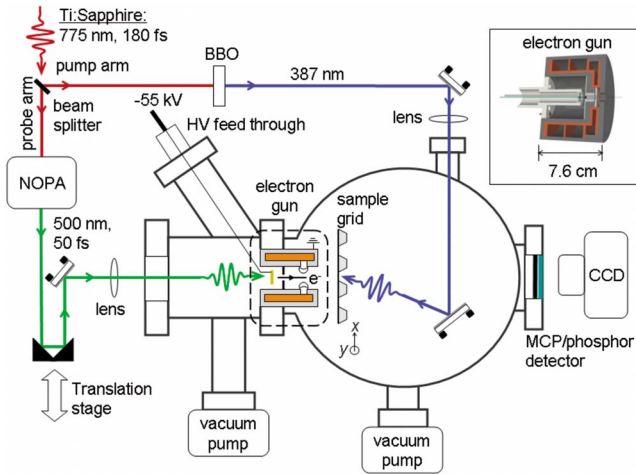


FIG. 1. (Color online) Schematic of the FED setup. The pump and probe arms are based on a Ti:Sapphire laser system with a fundamental wavelength of 775 nm. The frequency doubled pump pulse excites the free-standing Si sample mounted inside a vacuum chamber. The probe arm drives a noncollinear optical parametric amplifier, whose output at  $\sim 500$  nm is used to generate electrons from an Au photocathode via two photon photoemission. Electrons are accelerated to 55 keV and focused with a magnetic lens before scattering off the free-standing Si sample  $\sim 3$  cm away from the photocathode. The diffracted electrons are amplified using a micro-channel plate (MCP) system and detected on a phosphor screen. Timing between the electron probe and the laser pump is varied by changing the optical path length of the probe arm using a translation stage. Inset is detailed view of the electron gun section (representing the dashed box in the main figure) showing the cathode-anode assembly enclosed within the magnetic lens (iron shielding and copper core). A MACOR holder (white structure) electrically insulates the photocathode from the grounded magnetic-lens housing. The compact feature of the design allows generating electron pulses with  $<200$  fs duration and sufficient flux to probe structural changes with only a few pulses per time point.

and focuses the diffraction to specific lattice plane motions. Using this approach, it is possible to resolve impulsively driven phonon displacements on the femtosecond and longer time scales, and correlate the atomic motions to electron-phonon couplings. For the acoustic-phonon branch, the high-frequency cutoff is determined by the relaxation processes driving the acoustic modes and the thickness of the resonantly excited nanostructure, in this case a free-standing 33 nm Si film.

## II. EXPERIMENTAL SETUP

Our experimental setup is schematically shown in Fig. 1. The laser source for the time resolved FED studies is based on a fs Ti:Sapphire regenerative amplifier laser system where the 775 nm output is split into pump and probe arms. The frequency doubled pump arm at 387 nm is used to excite the single-crystal Si membrane, while the probe arm drives a noncollinear optical parametric amplifier (NOPA), whose output at 500 nm is used to generate electrons via two-photon photoemission from a gold photocathode. Photoemit-

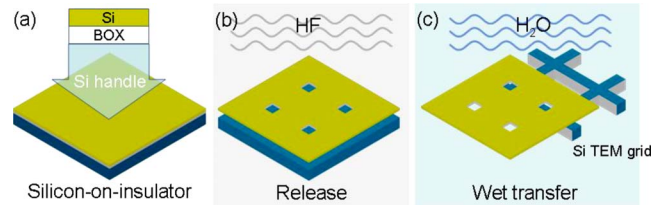


FIG. 2. (Color online) Schematics of the sample fabrication steps (not to scale). (a) A silicon-on-insulator piece where the top Si layer was thinned down to 33 nm by controlled oxidation and etching with HF. (b) The Si layer is released from the wafer handle via sacrificial etching of the buried-oxide layer. The holes shown in the film are used to facilitate the etching. (c) The released layer is picked up with a Si TEM grid.

ted electrons are accelerated to 55 keV by a dc field and focused with a magnetic lens before scattering off the Si membrane. The diffraction pattern is detected on a phosphor screen and captured with a charge-coupled device (CCD) camera. By changing the path difference between optical pump and electron probe, photoinduced structural changes in the sample are captured at specific time points relative to excitation. The inset of Fig. 1 shows the fs electron source, with photocathode, anode, and magnetic lens. An important feature of this design is the compactness of the electron gun. By limiting the total propagation distance of electrons to  $\sim 3$  cm, space-charge effects are considerably reduced, and shorter pulse durations are achieved. For the current study, the system was configured to deliver pulses that are  $\sim 300$  fs in duration at the sample position and contain  $\sim 10\,000$  electrons. The electron pulse duration is measured using the recently developed electron-laser cross-correlation technique based on ponderomotive scattering.<sup>17</sup>

An important aspect of the current experiment is the preparation of the free-standing Si films that are the subject of this investigation. The main fabrication steps are outlined in Fig. 2. First, the desired sample thickness is achieved by thinning the 200 nm outer Si layer of a commercially available silicon-on-insulator (SOI) wafer through controlled oxidation followed by etching in hydrofluoric acid (HF) [Fig. 2(a)]. The  $33 \pm 1$  nm thickness of the Si layer was verified using x-ray diffraction. Etch holes are next created in the Si film through a combination of photolithography and reactive ion etching. The thin film is subsequently separated from the Si handle wafer by etching of the buried-oxide (BOX) layer with HF [Fig. 2(b)]. Finally, the film is transferred onto a TEM grid made of Si [Fig. 2(c)]. We note that the Si TEM grids used as supporting structure were specifically fabricated for this kind of experiment. The advantage over commercially available copper TEM grids is the optical flatness and stiffness of the Si grid, which is necessary to ensure that the arrival time of the laser pump pulse relative to the electron probe pulse is well defined over the whole sample area. Additional details on the sample fabrication method are found in Refs. 18 and 19.

## III. RESULTS

The (001)-oriented single-crystalline Si membrane was excited at an absorbed fluence of  $\sim 2$  mJ/cm<sup>2</sup>, correspond-

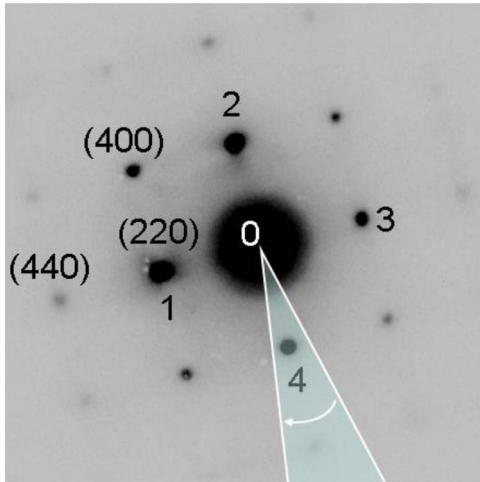


FIG. 3. (Color online) Diffraction pattern of the (001)-oriented single-crystalline Si membrane (inverted scale). To enhance the signal-to-noise ratio, intensity profiles of the individual diffraction spots are extracted by radially averaging over the appropriate image sector as shown here for the (220)-4 spot.

ing to a temperature rise of  $\sim 320$  K based on the heat capacity of bulk Si.<sup>20</sup> This excitation level is well below both the melting temperature of Si of 1693 K, and the  $\sim 6\%$  valence excitation threshold needed to electronically drive the lattice into disordering,<sup>21</sup> as it is estimated that under the current excitation conditions only  $\sim 0.6\%$  of the valence electrons are promoted to the conduction band. Diffraction images were captured at time delays ranging from  $-5$  to  $+115$  ps with a 1 ps step. Intensity profiles of the diffraction spots were constructed by radial averaging over the appropriate diffraction image sectors as shown in Fig. 3 for the (220)-4 spot. The extracted intensity profiles were then fitted to a Gaussian function with a linear baseline. Figure 4(a) shows the normalized diffracted intensities of the different (220) spots as a function of time delay. The dynamics display several interesting features: first, there is an initial fast change in intensity which amounts to  $\sim 20\%$  for the (220)-1

spot. Second, changes in intensity are accompanied by oscillations. Third, the four symmetric (220) diffraction spots exhibit dissimilar trends. Last, we observed no further changes in intensity when extending the experiment to 1.5 ns (using 30 ps steps). The latter feature indicates that after the change in intensity had developed (by  $\sim 100$  ps), the deposited energy lies entirely in the vibrational modes of the lattice (both coherent and incoherent). Cooling of the membrane back to room temperature occurs through heat diffusion via the bars of the supporting grid structure. By solving the heat diffusion equation  $\rho C \frac{\partial T}{\partial t} = \nabla \cdot (k \nabla T)$ , where  $\rho$ ,  $C$ , and  $k$  are, respectively, the density, heat capacity, and thermal conductivity of Si, we estimated the time scale for the cooling of the sample to be  $\sim 100$   $\mu$ s. Therefore, up to the  $\sim 1.5$  ns limit of the delay stage, it is valid to assume that no significant cooling occurs and the sample instead is characterized by the quasi-steady-state temperature estimated to be  $\sim 320$  K. In addition to the dynamics associated with the (220) order, the 0 order (center of diffraction pattern) exhibits a sharp decrease in intensity as shown in Fig. 4(b), indicating an overall increase in diffraction efficiency.

The dynamics described above cannot be explained by a change in the structure factor of the Si lattice. The structure factor of the (220) order is  $F_{220} = 8f$ , where  $f$  is the form factor of the Si atom. Because the conventional unit cell of Si has eight atoms, it is not possible under any lattice deformation to increase  $F_{220}$ , as it represents the maximum constructive interference. In addition, it is expected that under any lattice deformation the symmetry between the opposite 220 and  $\bar{2}20$  spots [labeled in Fig. 4(a) as 220-1 and 220-3] is preserved, as these correspond to reflections from the same set of lattice planes. This leads to an interesting question with respect to the operating mechanism for the observed enhancement in diffraction signal, which is clearly connected to acoustic modes of the crystal as is obvious from the strong modulation of the diffraction signal. Since changes in lattice structure are insufficient to explain our observations, we must consider other laser induced effects that lead to enhanced diffraction. The most plausible explanation is related to the angular dependence of the diffraction efficiency. The

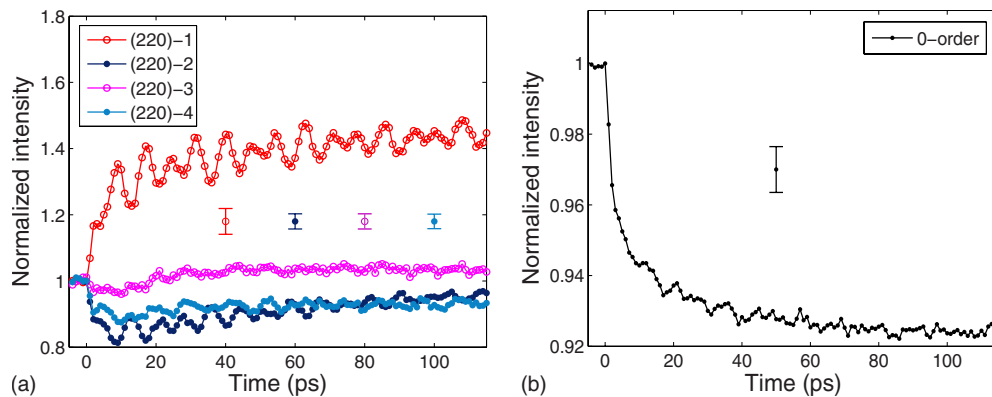


FIG. 4. (Color online) Electron-diffraction kinetics at  $\sim 2$  mJ/cm<sup>2</sup> excitation. (a) Photoinduced dynamics of each of the four (220) spots show an initial change in intensity (increase or decrease) accompanied by oscillations due to coherently driven acoustic phonons through fast carrier thermalization. Aside from the damping of the oscillations, no further changes in intensity levels were observed at time delays up to  $\sim 1.5$  ns. (b) The undiffracted spot (0 order) underwent an  $\sim 8\%$  decrease in intensity. The full length of the error bars in both panels represents twice the standard deviation of nine scans.

diffraction efficiency from a given plane is very sensitive to the angle of incidence of the electron beam and oscillates as a function of incident angle. Small changes in angle lead to accumulated phase differences along the propagation path that oscillate between constructive and destructive-interference effects in the diffraction process. Mathematically, this effect is related to the Bragg law for constructive interference from a set of lattice planes with an interplanar distance  $d$ ,  $2d \sin \theta = n\lambda$ , where  $\theta$  is the Bragg angle,  $n$  is the diffraction order, and  $\lambda$  is the de Broglie wavelength of the incident electrons. For 55 keV electrons, the Bragg condition for diffraction from the (220) planes is met at  $\theta = 0.76^\circ$ . In our geometry, the electron beam is incident near normal to the surface of the (001)-oriented Si film. Therefore, the Bragg condition cannot be simultaneously satisfied for all four symmetric (220) spots. This fact is reflected in the asymmetry of spot intensities of the static diffraction pattern shown in Fig. 3. Deviation from the Bragg condition is usually represented by the deviation vector  $s$  shown in Fig. 5(a) in the Ewald sphere construction. According to the dynamical diffraction theory, the variation in diffracted intensity as a function of  $s$  is given by

$$I_g = \frac{\sin^2[\pi L(s^2 + \xi_g^{-2})^{1/2}]}{\xi_g^2(s^2 + \xi_g^{-2})}, \quad (1)$$

where  $L$  is the sample thickness,  $g$  is the reciprocal-lattice vector at the Bragg condition, and  $\xi_g$  is the extinction distance.<sup>22</sup> The deviation  $\Delta\theta_i$  in angle of incidence is related to  $s$  by  $\Delta\theta_i \approx g \cdot s$ . The plot of  $I_g$  vs  $\Delta\theta_i$  shown in Fig. 5(b) reveals that a deviation as little as  $0.1^\circ$  could result in 50% change in diffracted intensity of the (220) order. In addition, changes in angle of incidence result in dissimilar trends for the opposite spots depending on the initial value of  $\theta$ . Based on this effect, we conclude that the observed changes in diffracted intensity are analogous to an x-ray rocking curve in which the effective planar rotation is optically induced by the Gaussian thermal distribution in the plane and the associated inhomogeneous transverse strain that develops from nonuniform thermal expansion. In all cases, the effect must be related to an increase in diffraction efficiency with increases in intensity of the (220)-1 spot. Increases in intensity of this diffraction order correlate to the depletion in the 0-order intensity as shown in Fig. 4(b). It is noted that the total detected intensity is conserved, as expected under this scenario.<sup>22</sup> Thus, the process must be due to changes in the acquired phase leading to constructive interference related to the (220) direction.

The dynamics of the intensity of the (220)-1 spot were analyzed first by performing a Fourier transform shown as the inset in Fig. 6. Two frequency components at 88 and 132 GHz were extracted, equivalent to the periods of oscillation of 11.4 and 7.6 ps, respectively. As the periods of these breathing modes correspond to round-trip acoustic-propagation normal to the film surface, the corresponding velocities of sound are  $5800 \pm 200$  and  $8700 \pm 300$  m/s, respectively. The error bars arise from the 1 nm uncertainty in the thickness of the film. These values are in excellent agreement with the velocities of the transverse and longitudinal

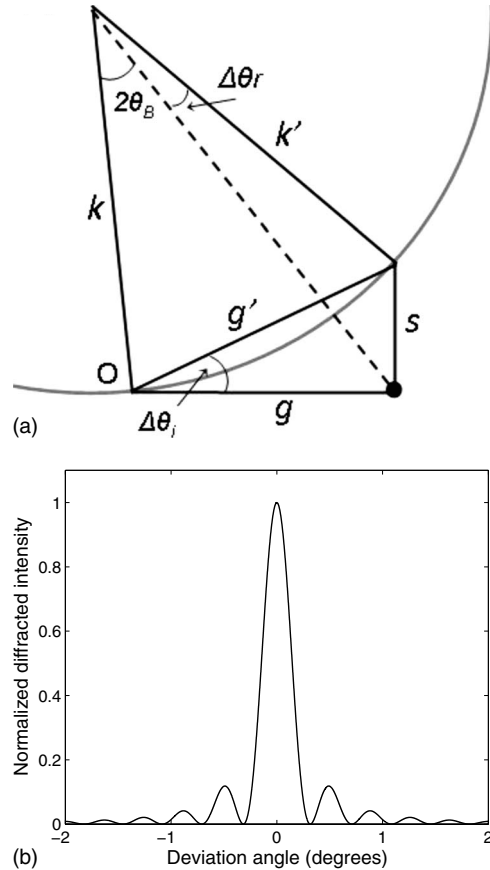


FIG. 5. Effect of change in electron angle of incidence on the diffracted intensity. (a) Ewald sphere construction showing the deviation from the ideal Bragg condition (adapted from Ref. 22). Normally, the diffraction condition is satisfied if the scattering vector  $g' = k' - k$  falls on a reciprocal-lattice point, ensuring the conservation of both energy and momentum. Here, the lattice (and consequently the reciprocal lattice) is rotated by angle  $\Delta\theta_i$  leading to a deviation from the Bragg condition, characterized by the deviation vector  $s$  (see Ref. 23 for a thorough description of how  $s$  is constructed). Because the reciprocal-lattice points are in reality rods with length inversely proportional to the crystal thickness, intersection of the Ewald sphere with these rods allows diffraction to occur even when the Bragg condition is not exactly satisfied. (b) The variation in the diffracted intensity of the (220) order of Si, as a function of  $\Delta\theta_i$  for a 33 nm thick crystal. The calculation is based on the dynamical diffraction theory. Note that the variation in detected angle  $\Delta\theta_r$  can be neglected (Ref. 23).

[001] acoustic modes, respectively, calculated from  $(C_{44}/\rho)^{1/2} = 5850$  m/s, and  $(C_{11}/\rho)^{1/2} = 8440$  m/s, where  $C_{11}$  and  $C_{44}$  are the elastic-stiffness constants of the Si lattice.<sup>24</sup> We next fitted the kinetics of the (220)-1 spot in the time domain to a function composed of a biexponential rise and two exponentially damped sine functions with fixed frequencies (Fig. 6), and extracted a damping time constant of  $\sim 100$  ps for both modes. Because the dynamics are complex, the biexponential fit we have used is meant to be phenomenological. It attempts to capture features from the following three contributions: (1) the Debye-Waller effect, which reflects the direct heating of the structure.<sup>25,26</sup> (2) The damping of oscillations, which transfers energy from the co-

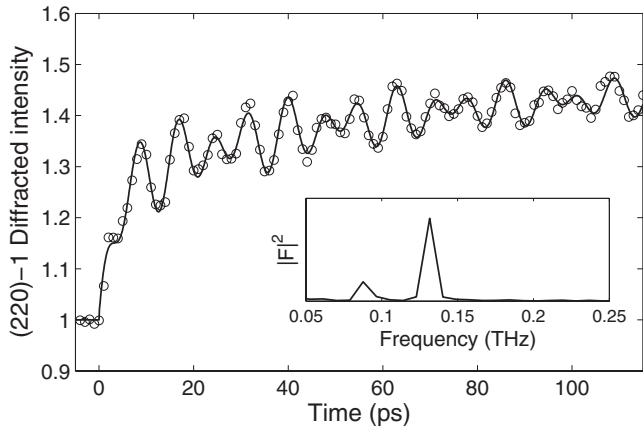


FIG. 6. Kinetics of the (220)-1 spot (circles) along with a fit that includes a biexponential rise component and two damped sinusoidal functions (solid line). The Fourier transform of the kinetics (inset) reveals the existence of two modes at 132 GHz (corresponding to the longitudinal polarization of the [100] acoustic waves) and at 88 GHz (corresponding to the transverse polarization of the [100] acoustic waves).

herent vibrational modes to a distribution of incoherent modes, effectively acting as an extra heating source. (3) Delayed heating due to Auger recombination.<sup>25</sup>

#### IV. DISCUSSION

The main issue is the mechanism through which the coherent acoustic phonons are generated. The sample is thin relative to the optical penetration depth ( $\sim 50$  nm) and carrier diffusion length over the time scale of excitation. Therefore, with respect to the longitudinal direction defined by the surface normal, there should be uniform excitation and thus uniform thermal deposition of energy into the acoustic modes. To first approximation, the crystal should uniformly expand along the surface normal. This process does not lead to coupling to transverse-acoustic modes and should not lead to changes in the in-plane atomic position as needed to observe the acoustics. So both the observation of the longitudinal-acoustic phonons and the generation of a transverse or shear acoustic phonons appear to contradict the assumed initial boundary conditions. These apparently unusual observations are related to the sample geometry and excitation conditions. This is because in our geometry thermal expansion is constrained in-plane both by the Gaussian temperature gradient due to the pump profile and by the supporting grid structure of  $120 \mu\text{m}$  periodicity. Herein lie the key details of the proposed mechanism. The sample has a Gaussian excitation profile in the transverse direction as defined by the laser spot size. The subsequent nonuniform heating upon carrier relaxation mimics this initial excitation profile as carrier diffusion is not sufficient over the length scale of the laser beam diameter to wash out the thermal gradient. The unbounded surfaces then undergo a uniform longitudinal expansion coupled to a nonuniform transverse stress that results in surface bulging. This nonuniform surface expansion leads to the coupling between longitudinal and transverse-

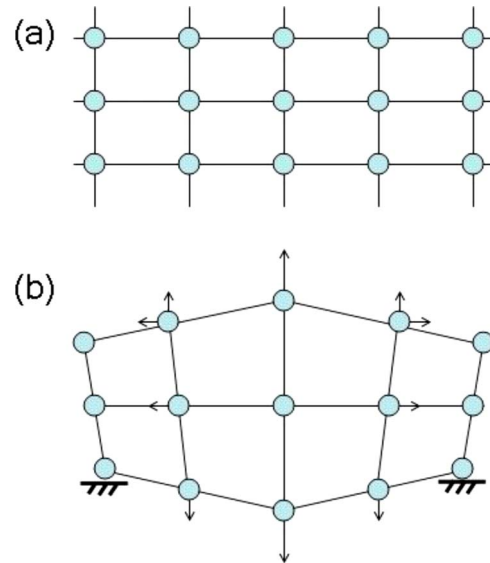


FIG. 7. (Color online) Schematic representation of the thermoelastic deformation of the Si membrane. (a) The initially unexcited lattice. (b) The Gaussian profile of the optical-pump pulse combined with the fixed boundaries at the supporting grid structure result in a nonuniform surface deformation with a shear component. These displacements lead to concerted excitation of both longitudinal and transverse-acoustic phonons.

acoustic components. The deformation imposes a nonlinear boundary condition on the problem, such that it is no longer possible to define a constant surface position. The problem is more complex as the underlying support grid is on a similar length scale to the excitation beam diameter. Therefore, the treatment of the initial stress-strain relationships becomes nontrivial.<sup>27</sup> Suffice it to say that the main result of nonuniform laser heating and periodic fixed boundary conditions from the grid supports in the transverse direction is accentuated nonuniform surface deformation (see Fig. 7 for a depiction of the deformation). Here, we note that the nanometer scale thickness of the samples as required for electron diffraction play an important role in these observations. The surface deformation contribution to the photoinduced acoustics would be negligible for thicker samples. This effect, however, will still be present and even more pronounced for surface probes and should be considered for electron diffraction in reflection geometry where surface effects are known to dominate.

The shear component of the deformation appears as a change in the intensity of the different (220) spots shown in Fig. 4(a). While a  $\sim 0.1^\circ$  shear deformation has negligible effect on the interplanar distances and structure factor of the lattice, it has a drastic effect on the diffracted intensities of the (220) spots due to deviation in the angle of incidence as shown previously. The initial stress is also responsible for the launching of both the longitudinal and shear acoustic phonons. While the initiation of the longitudinal mode is not unusual, thermoelastic excitation of shear oscillations usually requires crystals asymmetrically cut at  $>20^\circ$  to be observed optically.<sup>4,5</sup> The fact that we are able to observe transverse-acoustic modes without such projections in the observed strain fields is due to the stronger excitation conditions<sup>28</sup> and

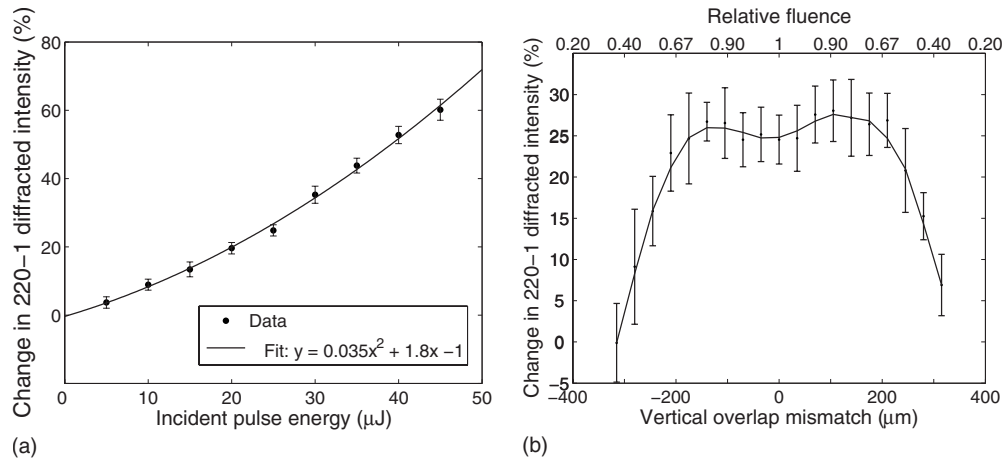


FIG. 8. Fluence and overlap dependence measurements. (a) Dependence of the change in diffracted intensity of the (220)-1 spot at  $\sim 100$  ps on the energy of the excitation pulse. The data are well described by a second-order polynomial (solid line). (b) Dependence of the change in diffracted intensity of the (220)-1 spot at  $\sim 100$  ps, on the offset between pump and probe beams at a fixed pump energy. The solid line is guide to the eyes.

the extremely sensitive detection method. Electron diffraction does not probe spatially averaged collective changes in optical properties as is the case in optical measurements of acoustic phonons. Rather, the observation involves an interferometric measurement of the relative atomic positions. The de Broglie wavelength of the probe electrons is much less than the interatomic spacing and strongly scatters from even minute changes in the atomic electron densities. The acquired phase differences as the electron propagates through the lattice greatly amplify the detection of the acoustic modes and provide direct information on the collective atomic displacements.

To verify the proposition that thermoelastic deformation is directly responsible for the observed effect, we performed the following control experiments. First, the fluence dependence of the observed effect was determined by exciting the sample at a range of incident pulse energies while observing the quasi-steady-state change in the (220)-1 diffracted spot intensity. The results, shown in Fig. 8(a), display a quadratic contribution to the dependence on incident fluence. This nonlinearity is another indication that the observed effect is not directly related to thermal or electronic stress, as in this regime both effects depend linearly on excitation. Next, we explored the pump-probe overlap dependence by probing the dynamics for various displacement offsets between electron probe and laser pump. Figure 8(b) shows the changes in diffracted intensity of the (220)-1 spot at  $\sim 100$  ps as a function of the relative offset between pump and probe. The calculated relative fluence (top  $x$  axis) at a specific offset (bottom  $x$  axis), was obtained by integrating the product of the Gaussian pump [600  $\mu\text{m}$  full width at half maximum (FWHM)] and probe (160  $\mu\text{m}$  FWHM) profiles for that offset. Maximum excitation corresponds to a perfectly aligned pump and probe beams (0 offset). However, this position does not correspond to maximum change in diffracted intensity or acoustic modulation of the (220)-1 spot. Instead, the curve in Fig. 8(b) appears to have a nearly flat profile around the center even though regions excited by the edges of the pump experience  $\sim 33\%$  less excitation due to the overlap

mismatch. This observation is a clear indication that the dynamics are not directly related to changes in lattice temperature or relative amount of strain developed in the longitudinal direction, but rather to thermoelastic deformation in the transverse direction. The amplitude of the transverse displacements is greatest at the spatial positions at which the thermal gradients in the in-plane direction are largest as observed. This motion causes changes in the relative transverse positions of the atoms and effectively a slight rotation of one plane relative to another in support of the nonuniform surface deformation. As the probed lattice planes rotate, the diffraction efficiency undergoes a net modulation. We note here that one is directly observing changes in atomic positions through changes in diffraction efficiency. The motions of the atoms are much smaller than can be resolved by extracting changes in the diffracted peak positions. With a full treatment of the phase dependence on electron propagation, the modulation in electron-diffraction efficiency can be directly correlated with the amplitude of the atomic motions and thus gives a direct measure of electron-phonon coupling. We expect similar observations to be possible for optical phonons and molecular vibrations in molecular crystals using shorter electron pulses and excitation processes that impulsively drive nonpropagating atomic displacements. In other words, it should be possible to directly observe the atomic motions of vibrational and collective modes.

Finally, it should be mentioned that in semiconductors, electronic stress due to the excitation of dense electron-hole plasma is expected to contribute to the initiation of the acoustic strain waves. The contribution of electronic stress relative to thermal stress under reversible conditions is in general independent of the excitation level, and is given by

$$\frac{\sigma_{el}}{\sigma_{th}} = \frac{C}{3\beta} \frac{dE_g}{dP} \frac{1}{(E - E_g)}, \quad (2)$$

where  $C$  is the heat capacity,  $\beta$  is the linear coefficient of thermal expansion,  $dE_g/dP$  is the pressure dependence of the energy gap, and  $E$  is the energy of the incident photon.<sup>1</sup> For

Si,  $\sigma_{el}/\sigma_{th} \approx -2$ , indicating that electronic stress should play a key role in photoacoustic generation. A recent study by Sondhauss *et al.*,<sup>29</sup> however, reported the contribution of electronic stress in InSb to be an order of magnitude less than expected from the above expression. Sondhauss *et al.* argued that rapid Auger recombination and diffusion of carriers act to reduce the electronic stress in just a few picoseconds following excitation. This prediction is supported by our earlier study on the heating dynamics of polycrystalline Si, in which we estimated that 66% of the carriers had recombined in the first 2 ps following excitation.<sup>25</sup> In principle, it is possible to separate the two effects based on the different dynamics for the two different source terms for the induced stress. The electronic stress develops instantaneously; whereas the thermal response takes on the order of 2 ps or longer for carrier thermalization. The slower thermally generated stress strain would manifest itself as a phase shift in the acoustic modulation.<sup>30</sup> The present signal to noise for a modulation period of approximately 10 ps is insufficient to observe this difference. This shortcoming does not affect the interpretation of the results since both stress contributions (electronic and thermal) have a Gaussian lateral profile following the excitation profile and both act as source terms in driving the acoustic modes.

## V. SUMMARY

We demonstrated the direct excitation of longitudinal and transverse coherent phonons in the  $\sim 100$  GHz frequency range in 33 nm free-standing single-crystalline Si. It was shown that the observed dynamics encompass three levels of complexities: first, a cascade of carrier and phonon relaxation processes occur in response to optical excitation of the semiconductor. Second, the lattice subsequently deforms due to thermoelastic and possibly some contribution from electronic stress. Third, the diffracted intensity is modulated due to the effective rotation of the lattice planes relative to the incident electron beam. Because of the nonlinear boundary

conditions imposed by the supporting grid structure and the inhomogeneous lateral temperature profile, extracting the stress-strain state of the film by solving the equations of elasticity is nontrivial. Nonetheless, the longitudinal and transverse coherent oscillations were resolved with good signal-to-noise ratio due to the high sensitivity of the technique. This sensitivity is reflected in the fact that the employed Si crystals had the [001] axis nearly perpendicular to the film surface ( $<0.2^\circ$  of miscut), which is in contrast with the large off-axis cuts needed to enhance the initiation of the shear mode in optical studies.<sup>4,5</sup> The quality of the data with respect to the detection of collective phonons is similar to all-optical measurements. However, with this technique it was possible to obtain an atomic perspective of the motion rather than a spatially averaged, modulated, optical property. Given the rising interest in ultrafast acoustic probing as a nondestructive diagnostic tool of nanosized structures, the current work provides a technique for the study of the mechanical properties of matter confined to nanoscale dimensions. By using this approach, it should also be possible to observe impulsively driven optical phonons and molecular vibrations at even higher frequencies with the correct crystal orientations, leading to an atomic perspective of relaxation pathways from optical-phonon to acoustic-phonon branches within the solid state.

## ACKNOWLEDGMENTS

We thank P. Evans for suggesting the collaboration between the groups, A.-A. Dhirani for use of his deposition chamber, G. Celler (Soitec, USA) for advice and for supplying SOI materials, and S. Gracewski, E. Sherman, and A. Cavalleri for helpful discussions. This work was supported by the Natural Sciences and Engineering Research Council of Canada. Support for the University of Wisconsin effort was provided by the U.S. National Science Foundation/MRSEC, Grant No. DMR0520527 and the U.S. Department of Energy, Grant No. DE-FG02-03ER46028.

\*Present address: Max-Planck-Institute of Quantum Optics, D-85748 Garching, Germany.

†dmiller@lphys.chem.utoronto.ca

<sup>1</sup>C. Thomsen, H. T. Grahn, H. J. Maris, and J. Tauc, *Phys. Rev. B* **34**, 4129 (1986).

<sup>2</sup>H. T. Grahn, H. J. Maris, and J. Tauc, *IEEE J. Quantum Electron.* **25**, 2562 (1989).

<sup>3</sup>P. Basseras, S. M. Gracewski, G. W. Wicks, and R. J. D. Miller, *J. Appl. Phys.* **75**, 2761 (1994).

<sup>4</sup>T. Pezeril, P. Ruello, S. Gougeon, N. Chigarev, D. Mounier, J.-M. Breteau, P. Picart, and V. Gusev, *Phys. Rev. B* **75**, 174307 (2007).

<sup>5</sup>O. Matsuda, O. B. Wright, D. H. Hurley, V. E. Gusev, and K. Shimizu, *Phys. Rev. Lett.* **93**, 095501 (2004).

<sup>6</sup>T. Pezeril, V. Gusev, D. Mounier, N. Chigarev, and P. Ruello, *J. Phys. D* **38**, 1421 (2005).

<sup>7</sup>C. Rossignol, J. M. Rampnoux, M. Pertion, B. Audoin, and S.

Dilhaire, *Phys. Rev. Lett.* **94**, 166106 (2005).

<sup>8</sup>K. A. Nelson, *J. Appl. Phys.* **53**, 6060 (1982).

<sup>9</sup>S. Nie, X. Wang, H. Park, R. Clinite, and J. Cao, *Phys. Rev. Lett.* **96**, 025901 (2006).

<sup>10</sup>C. Rose-Petrucci, R. Jimenez, T. Guo, A. Cavalleri, C. W. Siders, F. Rksi, J. A. Squier, B. C. Walker, K. R. Wilson, and C. P. J. Barty, *Nature (London)* **398**, 310 (1999).

<sup>11</sup>A. M. Lindenberg, I. Kang, S. L. Johnson, T. Missalla, P. A. Heimann, Z. Chang, J. Larsson, P. H. Bucksbaum, H. C. Kapteyn, H. A. Padmore, R. W. Lee, J. S. Wark, and R. W. Falcone, *Phys. Rev. Lett.* **84**, 111 (2000).

<sup>12</sup>A. Cavalleri, C. W. Siders, F. L. H. Brown, D. M. Leitner, C. Tóth, J. A. Squier, C. P. J. Barty, K. R. Wilson, K. Sokolowski-Tinten, M. von der Linde, M. Kammler, and M. Horn von Hoegen, *Phys. Rev. Lett.* **85**, 586 (2000).

<sup>13</sup>J. Larsson, A. Allen, P. H. Bucksbaum, R. W. Falcone, A. Lindenberg, G. Naylor, T. Missalla, D. A. Reis, K. Scheidt,

- A. Sjogren, P. Sondhauss, M. Wulff, and J. S. Wark, *Appl. Phys. A: Mater. Sci. Process.* **75**, 467 (2002).
- <sup>14</sup>M. Bargheer, N. Zhavoronkov, Y. Gritsai, J. C. Woo, D. S. Kim, M. Woerner, and T. Elsaesser, *Science* **306**, 1771 (2004).
- <sup>15</sup>A. Morak, T. Kämpfer, I. Uschmann, A. Lübcke, E. Förster, and R. Sauerbrey, *Phys. Status Solidi B* **243**, 2728 (2006).
- <sup>16</sup>U. Shymanovich, M. Nicoul, J. Blums, K. Sokolowski-Tinten, A. Tarasevitch, T. Wietler, M. Horn von Hoegen, and D. von der Linde, *Appl. Phys. A: Mater. Sci. Process.* **87**, 7 (2007).
- <sup>17</sup>C. T. Hebeisen, G. Sciaini, M. Harb, R. Ernstorfer, T. Dartigalongue, S. G. Kruglik, and R. J. D. Miller, *Opt. Express* **16**, 3334 (2008).
- <sup>18</sup>M. Roberts, L. J. Klein, D. E. Savage, K. A. Slinker, M. Friesen, G. Celler, M. A. Eriksson, and M. G. Lagally, *Nature Mater.* **5**, 388 (2006).
- <sup>19</sup>S. A. Scott and M. G. Lagally, *J. Phys. D* **40**, R75 (2007).
- <sup>20</sup>P. D. Desai, *J. Phys. Chem. Ref. Data* **15**, 967 (1986).
- <sup>21</sup>M. Harb, R. Ernstorfer, C. T. Hebeisen, G. Sciaini, W. Peng, T. Dartigalongue, M. A. Eriksson, M. G. Lagally, S. G. Kruglik, and R. J. D. Miller, *Phys. Rev. Lett.* **100**, 155504 (2008).
- <sup>22</sup>P. E. Champness, *Electron Diffraction in the Transmission Electron Microscope*, Garland Science, 1st ed. (BIOS Scientific Publishers, Oxford, UK 2001).
- <sup>23</sup>H. Hashimoto, *J. Phys. Soc. Jpn.* **9**, 150 (1954).
- <sup>24</sup>C. Kittel, *Introduction to Solid State Physics* (Wiley, New York, 1986).
- <sup>25</sup>M. Harb, R. Ernstorfer, T. Dartigalongue, C. T. Hebeisen, R. E. Jordan, and R. J. D. Miller, *J. Phys. Chem. B* **110**, 25308 (2006).
- <sup>26</sup>E. J. Yoffa, *Phys. Rev. B* **23**, 1909 (1981).
- <sup>27</sup>The difficulty in solving the equations of elasticity is also due to three-dimensional character of the problem. The one-dimensional problem, which is relevant to experiments where the only excited mode is the longitudinal, has an analytic solution derived by Thomson *et al.* (see Ref. 1). To our knowledge, the only treatment of the three-dimensional problem is the one proposed by Pezeril *et al.* (Refs. 4 and 6). However, these are for different geometries and boundary conditions than the free-standing film.
- <sup>28</sup>Although we excite the sample at  $\sim 320$  K, the thermal-expansion coefficient of Si of  $2.6 \times 10^{-6} \text{ K}^{-1}$  is approximately ten times smaller than that of elements examined in other studies. For example, in Zn the *c*-axis coefficient is  $6.4 \times 10^{-5} \text{ K}^{-1}$  and the one along the perpendicular is  $1.3 \times 10^{-5} \text{ K}^{-1}$  (Ref. 5). Therefore, this strong excitation is needed to generate sufficient strains to observe the effect.
- <sup>29</sup>P. Sondhauss, O. Synnergren, T. N. Hansen, S. E. Canton, H. Enquist, A. Srivastava, and J. Larsson, *Phys. Rev. B* **78**, 115202 (2008).
- <sup>30</sup>L. Genberg, Q. Bao, S. Gracewski, and R. J. D. Miller, *Chem. Phys.* **131**, 81 (1989).